

Accepted Article Preview: Published ahead of advance online publication



Microcavity-Enhanced Optoelectronic Fiber Photoacoustic Spectroscopy for ppb-Level Trace Gas Sensing

Yanyu Jiang, Minghui Du, Xile Han, Zhuobei Deng, Jie Mao, Liang Chen, Yifan Wang, Ying Liu, Yafei Li, Ruohui Wang, Chuantao Zheng and Tuan Guo

Cite this article as: Yanyu Jiang, Minghui Du, Xile Han, Zhuobei Deng, Jie Mao, Liang Chen, Yifan Wang, Ying Liu, Yafei Li, Ruohui Wang, Chuantao Zheng and Tuan Guo. Microcavity-Enhanced Optoelectronic Fiber Photoacoustic Spectroscopy for ppb-Level Trace Gas Sensing. *Light: Advanced Manufacturing* accepted article preview article preview 10 February, 2026; doi: 10.37188/lam.2026.028

This is a PDF file of an unedited peer-reviewed manuscript that has been accepted for publication. LAM are providing this early version of the manuscript as a service to our customers. The manuscript will undergo copyediting, typesetting and a proof review before it is published in its final form. Please note that during the production process errors may be discovered which could affect the content, and all legal disclaimers apply.

Received 3 August 2025; revised 16 January 2025; accepted 25 January;
Accepted article preview online 10 February 2026

Microcavity-Enhanced Optoelectronic Fiber Photoacoustic Spectroscopy for ppb-Level Trace Gas Sensing

Yanyu Jiang^{1†}, Minghui Du^{1†}, Xile Han^{1†}, Zhuobei Deng², Jie Mao¹, Liang Chen¹, Yifan Wang¹, Ying Liu¹, Yafei Li^{2*}, Ruohui Wang^{3*}, Chuantao Zheng^{4*}, Tuan Guo^{1*}

¹ Institute of Photonics Technology, College of Physics & Optoelectronic Engineering, Jinan University, Guangzhou 510632, China

² College of Information Science and Technology, Jinan University, Guangzhou 510632, China

³ School of Physics, Northwest University, Xian 710127, China

⁴ The State Key Laboratory of Integrated Optoelectronics, College of Electronic Science and Engineering, Jilin University, Changchun, 130012, China

Abstract— Photoacoustic spectroscopy is a highly sensitive analytical technique for trace chemical detection in gaseous and liquid phases. Conventional systems relying on free-space optics face limitations in light-matter interaction efficiency and electronic integration. To address this, we developed a miniaturized, ultrasensitive photoacoustic spectroscopy gas sensor by integrating a thermally drawn multi-material optoelectronic fiber, a T-type resonant photoacoustic cell, and a MEMS microphone at the fiber tip. This system enables amplified light-gas interactions and simultaneous electrical signal acquisition, achieving ppb-level detection within seconds using sub-microliter sample volumes (0.02 mL). By leveraging mass-producible optoelectronic fibers and MEMS technology, this work establishes a new class of optical sensors featuring compact size, ultrahigh sensitivity, environmental robustness, and scalable multiplexed detection capabilities for harsh environments.

Keywords—Photoacoustic spectroscopy; Gas sensing; Optoelectronic fibers; MEMS

Correspondence: Y.L. (liyafei@jnu.edu.cn) or R.W. (rwang@nwu.edu.cn) or C.Z. (zhengchuantao@jlu.edu.cn) or T.G. (tuanguo@jnu.edu.cn)

These authors contributed equally: Yanyu Jiang, Minghui Du, and Xile Han

Introduction

Ultrasensitive gas sensors have broad application prospects in various fields, including the health monitoring of energy batteries [1–3], the detection of environmental pollutants [4,5], and the analysis of exhaled gases in biomedical [6–8]. Traditional electrochemical sensors based on gas-sensitive materials have gained significant attention due to their unique advantages, such as minimal sample requirements and rapid response times. However, this technology faces limitations in maintaining stability because of the sensitivity of gas-sensitive materials to poisoning effects. The optical gas detection technologies, such as fluorescence, gas chromatography, and infrared spectroscopy, exhibit exceptional sensitivity and selectivity, but their large size, high maintenance costs, and complex operational procedures considerably restrict the practicality in real-world applications. Therefore, developing ultrasensitive and miniaturized gas sensors with low cost and repeatability remains a significant challenge in current research.

Photoacoustic spectroscopy (PAS) has emerged as a leading approach for online trace gas detection due to its advantages of high sensitivity, excellent selectivity, and rapid response time [9–12]. Its core detection process relies on the selective absorption of lasers with specific wavelengths by gas molecules. Photoacoustic (PA) gas sensor detects sound waves generated by thermal expansion and contraction of gas molecules absorbing modulated light. Different from direct absorption spectroscopy [13], PAS uses a micro-electro-mechanical system (MEMS) microphone to detect acoustic signal related to gas concentration, eliminating the need for expensive infrared photodetectors and offering a background-free detection capability. Typically, the PA signal was measured in a PA cell. Gong et al. [14] proposed a T-type semi-open photoacoustic cell (PAC) with a volume of about 25 mL, achieving a limit of detection (LOD) of 0.7 parts per billion (ppb) for acetylene (C_2H_2) gas. Li et al. [15] designed a multi-channel Helmholtz-type cell, which achieved a LOD of 18 ppb for C_2H_2 with an integration time of 166 s. Zhao et al. [16] used a differential multi-pass cell with a volume of 162 mL and an optical path of 4.92 m to enhance the PA signal, achieving a minimum detection limit of 0.6 ppb for methane (CH_4).

However, the traditional PAS technique requires large-volume PA cell and complex external equipment, limiting its application in scenarios requiring rapid response, miniaturization, and precise monitoring [17,18]. With the development of micro spectroscopy technology, there is an increasing demand for intelligent sensors with miniaturization, integration and remote monitoring capability. MEMS microphones have been widely used as the PA signal collection devices due to their small size and high sensitivity. The transmission of electrical signals necessitates external circuitry, but the conventional optical fiber can only transmit optical signals, not electrical signals. The limitation complicates the integration and miniaturization of sensors [19–24]. Multimaterial thermal drawing technology enables the integration of diverse functional materials such as metals, semiconductors, crystals, glass, polymers, and even micro-devices into a single fiber, achieving multifunctional composite structures to meet various

application needs [25–27]. Combining the PA cell with the multimaterial optoelectronic fiber offers an ideal solution to the above challenges, paving the way for miniaturized optoelectronic gas detection devices.

In this study, we designed a PA gas sensor by integrating a multimaterial optoelectronic fiber, a T-PAC and a MEMS microphone. The sensor can achieve simultaneous transmission of pump light signals and detection electrical signals. Compared to traditional H-type longitudinal resonance PA cell, the designed T-PAC has a higher cell constant, faster response time, and a simpler fabrication process, while reducing the cavity volume to only 0.02 mL. The optical pathlength-to-volume ratio (OPVR) of the sensor is $1736.8 \text{ mm}\cdot\text{mL}^{-1}$. The experimental results show that the sensor has a low detection limit of 211 ppb and a response time of $\sim 3 \text{ s}$ for C_2H_2 gas. This work establishes a new class of optical sensors featuring compact size, ultrahigh sensitivity, environmental robustness, and scalable multiplexed detection capabilities for harsh environments.

Results

The structure of the designed PA gas sensor based on the multimaterial optoelectronic fiber is shown in Fig. 1a. Gas molecules diffuse into the miniature T-PAC, where they absorb pump light and generate acoustic waves. The acoustic waves are tightly confined by the T-PAC, which acts as a hard acoustic boundary, resulting in pressure levels several orders of magnitude higher than those of free-space-expanding PA waves. Simultaneously, the T-PAC resonance amplifies the pressure level of the acoustic waves. The excitation and demodulation scheme of the PA signals is illustrated in Fig. 1b, the center wavelength of the pump light was slowly scanned over the gas absorption line, and its frequency was sinusoidally modulated. The locally excited PA waves were amplified by the T-PAC and collected by a MEMS microphone, which were then converted into electrical signals. A lock-in amplifier was used to acquire the second harmonic ($2f$) signals of the PA signals to determine the gas concentration.

Assuming a frequency-modulated beam with the light intensity $I(r, t)$ and the frequency ν is incident into T-PAC. Gas molecules within the cell transition from the ground state to the excited state upon absorbing light energy, generating a thermal power density source $H(r, t)$, which can be expressed as [28]

$$H(r, t) = c\sigma I(r, t) = aI(r, t) \quad (1)$$

where c , σ and a are the concentration, absorption cross-section and absorption coefficient of the gas molecules, respectively. The light intensity $I(r, t)$ is frequency-modulated, so the thermal power density source $H(r, t)$ oscillates at the same frequency. Under the condition of unsaturated absorption, $H(r, t)$ is proportional to the gas concentration N when the light intensity $I(r, t)$ remain constant. According to the working mode of acoustic waves, PA cell includes resonant PA cell and non-resonant PA cell. Compared with the non-resonant PA cell, the resonant PA cell has higher sensitivity for trace gas detection. Utilizing the acoustic resonance of the PA cell is one of the effective means to increase the intensity of PA excitation. For a T-type PA cell, its first-order longitudinal acoustic mode $P_{(100T)}(\vec{r})$ and resonant frequency $f_{(100T)}$ can be written as [29, 30]

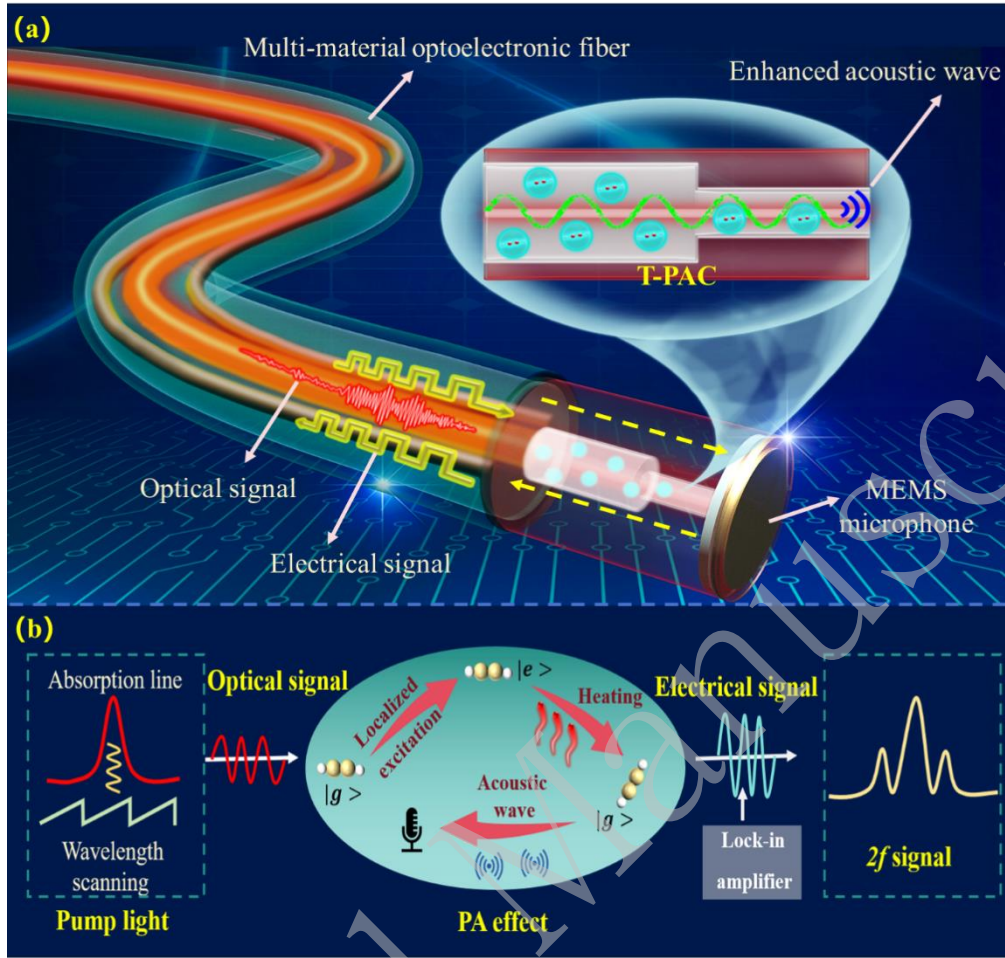


Fig. 1. (a) Structural schematic diagram and (b) PA gas sensing principal diagram of the high-integrated all-fiber sensor.

$$P_{(100T)}(\vec{r}) = \cos\left(\frac{\pi}{2L}z\right) \quad (2)$$

$$f_{(100T)} = \frac{s}{4L_{\text{eff}}} \quad (3)$$

where L is the geometric length of the resonant cavity, s is the speed of sound in the target gas, and z is the longitudinal coordinate. When $z=0$, $P_{(100T)}(\vec{r})=1$, the antinode of the standing wave is located at the end of the T-PAC away from the buffer cavity. When $z=L$, $P_{(100T)}(\vec{r})=0$, the node is at the interface between the resonant cavity and the buffer cavity^[31]. Assuming the radius of resonant cavity is R , the effective length L_{eff} can be written as

$$L_{\text{eff}} = L + \frac{16}{3\pi}R \quad (4)$$

When $R \ll L$, the resonant frequency $f_{(100T)}$ is approximately inversely proportional to L . When neglecting the viscous and the thermal losses of the gas, the periodic thermal power density source induces periodic pressure changes. The acoustic signal is converted into the electrical signal by an acoustic transducer, and the amplitude S_{PA} of the output signal can be expressed as^[32]

$$S_{\text{PA}} = S_0 P_{\text{eff}} F c \alpha = C_{\text{cell}} a P_{\text{eff}} \quad (5)$$

where S_0 is the sensitivity of the acoustic transducer ($\text{mV} \cdot \text{Pa}^{-1}$);

P_{eff} is the effective optical power (W); F is the cell constant ($\text{Pa} \cdot \text{cm}^{-1} \cdot \text{W}^{-1}$), it directly reflects the PAC's capability to enhance PA signals; c is the gas concentration (ppb); α is the gas absorption coefficient (cm^{-1}); C_{cell} represents the efficiency of light-to-sound energy conversion in the PA system.

Multimaterial optoelectronic fibers

Multimaterial optoelectronic fibers are fabricated using a scalable thermal drawing technique, which enables the integration of diverse functional materials such as glasses, metals, and polymers into a single fiber^[33-36]. During this process, macroscopic preforms with the desired material composition are heated to a softened state in a furnace and then drawn into kilometers-long fibers with micro- or nanoscale features under a pulling force, as illustrated in Fig. 2a. This technique allows precise control over the fiber's geometry and material distribution, facilitating the creation of complex architectures. In a typical fabrication process, an optoelectronic fiber composed of metal electrode, silica fiber, and polymer are thermally drawn. Two copper filaments and a silica fiber are fed into a polymethyl methacrylate (PMMA) cladding to form the final fiber. The fiber diameter is regulated by controlling the drawing temperature, drawing speed, preform feeding speed, and the initial diameter of the preform. As a result, fibers with diameters ranging from macroscale to microscale can be

successfully produced. The fabrication process is highly scalable, enabling the production of kilometers-long fibers within one hour. A bundle of drawn optoelectronic fibers is shown in Fig. 2b, while Fig. 2c displays the configuration with the central waveguide surrounded by two metal electrodes. The final fiber retains the geometry and composition of the macroscopic preform. The structure of the drawn fibers is highly intact, with the central silica fiber and copper electrodes closely adhering to the PMMA cladding. The polymer PMMA is used as the outer cladding material to integrate the metal electrodes and the glass fiber core. Specifically, the glass fiber core functions to transmit optical signals, while the copper electrodes are responsible for receiving electrical signals.

A unique advantage of this technique is the ability to precisely control the separation distance between the electrode and the central waveguide. As shown in Fig. 2d, the characteristic size of the fiber is gradually reduced in the neck-down region during the thermal drawing process. By fixing the feeding and drawing parameters, the separation distance D_2 scales linearly with the initial distance D_1 . Additionally, the arrangement of the electrode and waveguide can be easily adjusted. The

optoelectronic fiber exhibits excellent light transmission capabilities. As shown in Fig. 2e, the transmission spectra and corresponding images demonstrate high transmission (>90%) at the wavelength of 1550 nm. The fibers retain light transmission performance comparable to commercial single-mode fiber, indicating that the thermal drawing process does not compromise their performance. Furthermore, the internal silica fiber can be seamlessly integrated with commercial fiber systems without mode-field mismatch concerns.

The fabricated optoelectronic fiber also demonstrates excellent electrical properties due to the pure copper filaments uniformly distributed along the fiber's axial direction. The resistance of the fiber was measured using a multimeter, as shown in Fig. 2f. Owing to its metallic properties, the fiber's resistance shows minimal changes as the temperature increases from 20 °C to 60 °C, making it highly suitable for electrical signal collection and transmission. Additionally, the fabricated optoelectronic fibers are highly flexible. Its bending stiffness is evaluated over a frequency range of 0–100 Hz, as shown in Fig. 2g. The results reveal that stiffness of the fiber increases with the fiber diameter. The mechanical properties of the fiber can

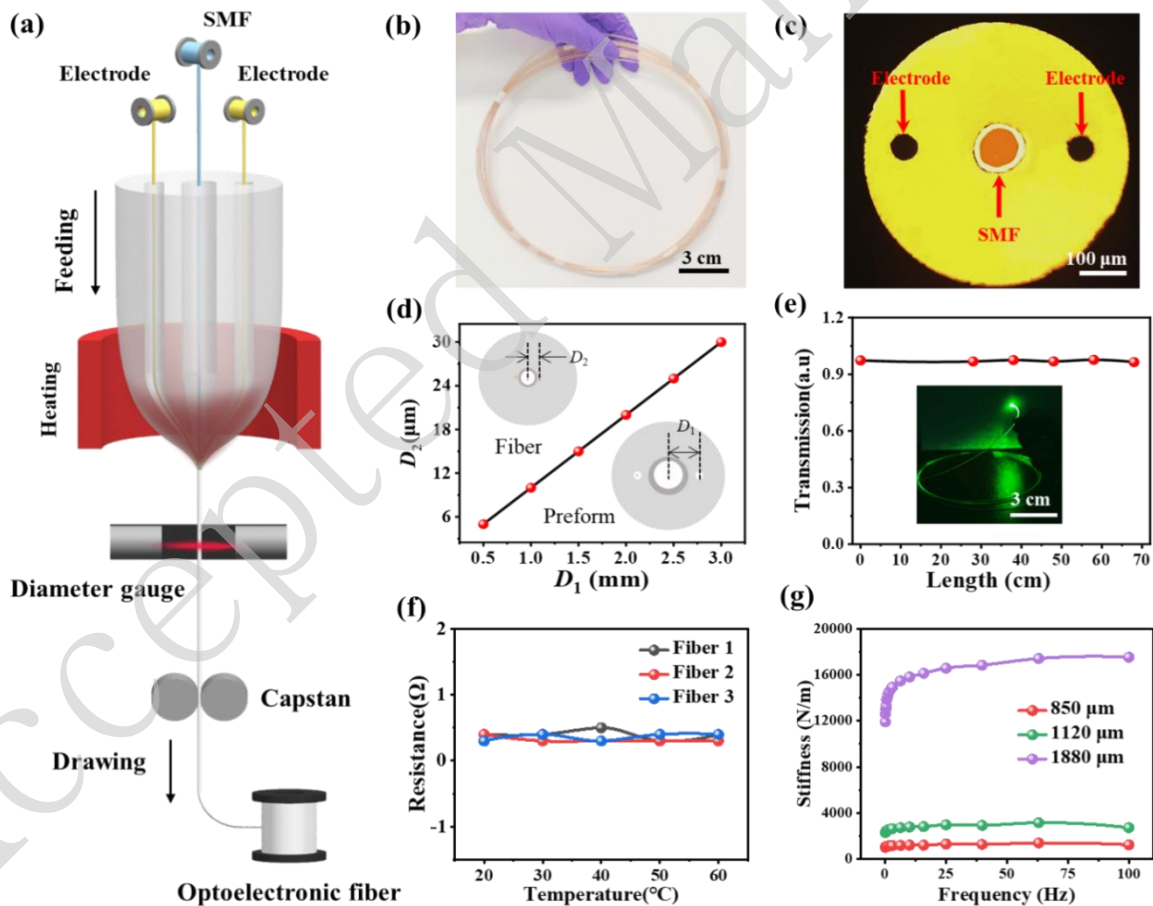


Fig. 2. Fabrication and characterization of multimaterial optoelectronic fiber. (a) Schematic of the thermal drawing process. (b) Photograph of the drawn optoelectronic fibers. (c) Optical image of cross-section of the drawn multimaterial optoelectronic fiber. (d) Linear dependence of the characteristic scale of the optoelectronic fiber on the pre-designed configuration after fixing the drawing parameters. (e) Transmission spectra of the optoelectronic fiber at different lengths at a wavelength of 1550 nm. The inset shows a photograph of fiber when it is excited by a 532 nm laser. (f) Correlation of electrical properties of optoelectronic fibers with temperature. Fiber 1, 2, 3 represents the fiber embedded with copper electrodes with diameters of 100, 200, 250 μm , respectively. (g) Mechanical stiffness of optoelectronic fiber as a function of frequency.

be further improved by optimizing the fiber diameter. The robust mechanical properties of the optoelectronic fiber make it an ideal candidate for next-generation flexible gas sensors capable of withstanding compressive or tensile stress.

Design and optimization of photoacoustic sensor

In low-frequency PA gas sensors, flicker noise ($1/f$ noise) dominates, and the resonant frequency $f_{(1007)}$ is approximately inversely proportional to the cavity length L . This conclusion assumes negligible optical transmission loss in the PA cell. Otherwise, the signal-to-noise ratio (SNR) degrades with increasing cavity length. Additionally, the cavity radius R has minimal impact on $f_{(1007)}$ compared to L , and the cell constant F is inversely proportional to R . A smaller R can improve SNR and increase viscous damping, so it is necessary to strike a balance between sensitivity and stability [37,38]. Fig. 3a illustrates a perspective view of the PA gas sensor, in which the T-PAC is integrated with the multimaterial optoelectronic fiber. The MEMS microphone is compactly embedded within the end structure of the T-PAC. The prepared optoelectronic fiber is soaked in a dichloromethane solution, which corrodes the PMMA material, and then soldering the exposed metal electrodes to the pins of the MEMS microphone. The electrode connection points are completely wrapped and sealed by the polymer matrix, isolating them from the external environment,

thereby completely avoiding issues such as oxidation and electrolytic corrosion, resulting in excellent stability.

To design high-integrated and miniaturized PA cell, the finite element method (FEM) simulations were employed to analyze the sound pressure magnitude of the buffer cavity and resonant cavity at varying radii and lengths by COMSOL software. In the simulations, the temperature was set to 300 K and the pressure was set to 1 atm. To ensure high integration with the multimaterial optoelectronic fiber, a ceramic insert with an inner diameter of 126 μm and an outer diameter of 1.25 mm was integrated onto the fiber end-face, therefore, the inner diameter of the buffer chamber is determined to be 1.25 mm. According to the theoretical derivation, the smaller the size, the greater the sound pressure, but reducing the radius also increases the noise level of the PA cell, so the radius should not be excessively small. In order to balance the sound pressure and noise, the length of the buffer chamber is set to 15 mm. Fig. 3b shows the sound pressure distribution of the resonant cavity at lengths of 16 mm, 18 mm and 20 mm. The wave belly and wave node are located at the two ends of the resonator, and the maximum sound intensity occurs at the top of the T-PAC. Therefore, the MEMS microphone should be mounted at the apex to capture the maximum PA signals. Fig. 3c shows the magnitudes of sound pressure and resonant frequency of the resonant cavity at different lengths. With the increase of length,

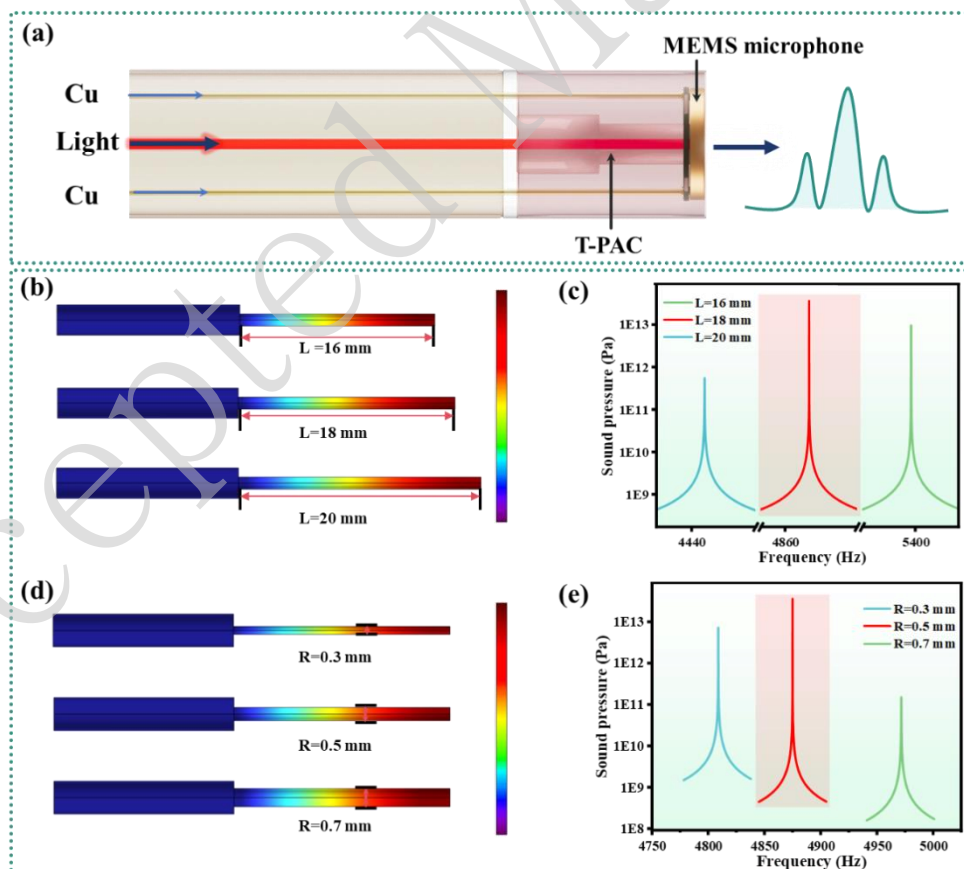


Fig. 3. (a) The structure diagram and sensing principle of the PA gas sensor. (b) The simulated sound pressure distribution of the resonant cavity at lengths of 16 mm, 18 mm and 20 mm. (c) The magnitudes of sound pressure and resonant frequency at different lengths. (d) The simulated sound pressure distribution of the resonant cavity at radii of 0.3 mm, 0.5 mm and 0.7 mm. (e) The magnitudes of sound pressure and resonant frequency at different radii.

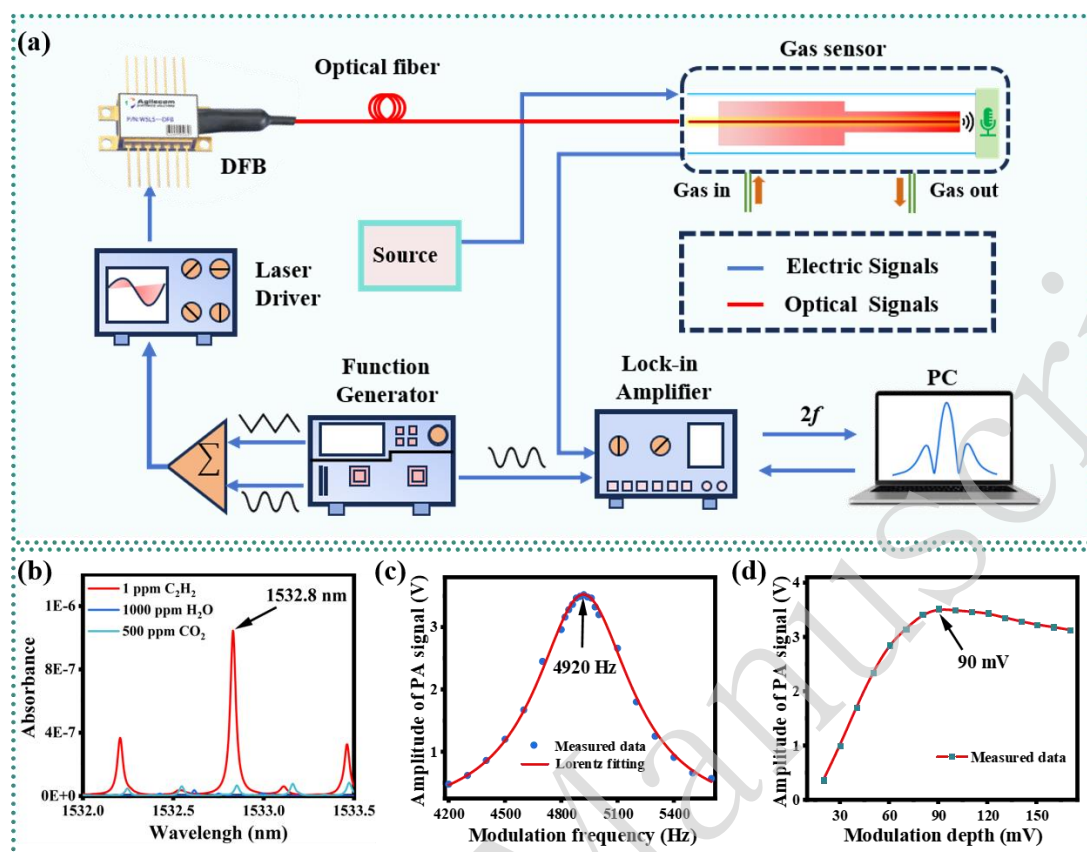


Fig. 4. (a) The structural diagram of the experimental system. (b) The absorbance of 1 ppm C₂H₂, 1000 ppm H₂O and 500 ppm CO₂ within the wavelength range of 1532 nm to 1533.5 nm. (c) The frequency response curve of the T-PAC within the range of 4200 Hz to 5600 Hz. (d) The relationship between the PA signal amplitude and the modulation depth.

the sound pressure first increases and then decreases, and the resonant frequency always decreases. Fig. 3d shows the sound pressure distribution of the resonant cavity at radii of 0.3 mm, 0.5 mm and 0.7 mm. Fig. 3e shows the magnitudes of sound pressure and resonant frequency of the resonant cavity at different radii. With the increase of radius, the sound pressure first increases and then decreases, and the resonant frequency keeps increasing. Considering the difficulty and precision of processing, the radius and the length of the resonant cavity were set to 0.5 mm and 18 mm, respectively, with a resonance frequency of 4875 Hz. It is worth mentioning that the total volume of the T-PAC is only 0.02 mL, significantly smaller than that of conventional PA cells.

Characterization of photoacoustic gas sensor

The structural diagram of the experimental system is depicted in Fig. 4a. Fig. 4b presents the absorbance of 1 part per million (ppm) C₂H₂, 1000 ppm H₂O and 500 ppm CO₂ within the wavelength range of 1532 nm to 1533.5 nm. To mitigate the interference effects of H₂O and CO₂ in the air, an excitation light wavelength of 1532.8 nm was selected for C₂H₂ detection. To achieve the maximum resonance effect, it is essential to perfectly match the modulation frequency of the laser with the resonant frequency of the T-PAC. Therefore, the modulation frequency of the laser was optimized prior to gas experiments. A gas flow controller was used to introduce 5000 ppm C₂H₂ gas

into the T-PAC. Fig. 4c displays the frequency response curve of the T-PAC within the range of 4200 Hz to 5600 Hz. It is evident that the PA signal amplitude reaches maximum when the resonant frequency of the T-PAC is 4920 Hz, corresponding to the modulation frequency of 2460 Hz for the laser. Therefore, the first resonant frequency of the T-PAC is determined to be 4920 Hz, which closely matches the simulated value of 4875 Hz. The discrepancies between the actual resonant frequency and simulated resonant frequency of T-PAC primarily stem from two factors: first, simulations rely on idealized geometric models, which do not account for material inconsistencies and manufacturing tolerances; second, real-world testing is susceptible to environmental factors like temperature, pressure, and humidity, which may introduce minor deviations. However, such subtle discrepancies are generally deemed acceptable in practical applications. To maximize the PA signal amplitude, the modulation depth of the laser was also optimized. Fig. 4d illustrates the relationship between the PA signal amplitude and the modulation depth. When the modulation depth is below 90 mV, the PA signal amplitude increases with the modulation depth. However, the PA signal amplitude no longer exhibits significant changes when modulation depth is beyond 90 mV. Therefore, the modulation depth of the laser was set to 90 mV.

The performance of the developed PA gas sensor through a series of experiments was evaluated. The PA signal amplitudes of the non-resonant PA cell and the T-PAC at a concentration of 2% C₂H₂ gas were compared under the same dimensions. As

shown in Fig. 5a, the $2f$ signal amplitudes of the non-resonant PA cell and T-PAC are 4.13 V and 13.44 V, respectively. Compared with the non-resonant cavity, the PA signal amplitude and the SNR of the T-PAC are improved by a factor of ~ 3.3 and ~ 7.0 , respectively. As shown in Fig. 5b, the repeatability of the sensor was evaluated by performing six response recovery cycles at a concentration of 0.3% C_2H_2 gas, and the result shows that the response remained almost constant after six cycles. As shown in Fig. 5c, the response time of the sensor was tested at a concentration of 0.3% C_2H_2 gas, and the results show that the rise time $T_{10\%-90\%}$ is 2.4 s and the fall time $T_{90\%-10\%}$ is 3.3 s, the PA cell structure can be optimized to shorten the diffusion path and accelerate the gas renewal process to further reduce the response time in the future. In order to evaluate the response characteristics of the developed gas sensor to C_2H_2 gas, C_2H_2 gas with concentrations of 0.3%, 0.5%, 1%, 1.5%, and 2% was prepared through the MFC, and then passed into the T-PAC at a

flow rate of 100 sccm. Fig. 5d shows the PA signal amplitudes at different C_2H_2 gas concentrations, and the PA signal amplitudes are relatively flat at the same concentration, which indicates a good stability of the sensor. Fig. 5e shows the waveforms of the extracted $2f$ signals at different C_2H_2 gas concentrations. In order to evaluate the relationship between the PA signal and gas concentration, a linear fit was used to show the trend of the responsivity. As shown in Fig. 5f, there is a linear relationship between the PA signal amplitudes and the C_2H_2 gas concentrations, with a responsivity of $0.667 \text{ mV}\cdot\text{ppm}^{-1}$. The R-squared value is estimated to be 0.999, which exhibits a very good linearity. Humidity is a key factor affecting the performance of the sensor. To evaluate the effect of humidity, the gas sensor was exposed to 0.3% C_2H_2 at room temperature, with relative humidity (RH) levels varying from dry to 80%, which is a typical range for non-rainy conditions. The uniform and stable relative humidity in the chamber is controlled by

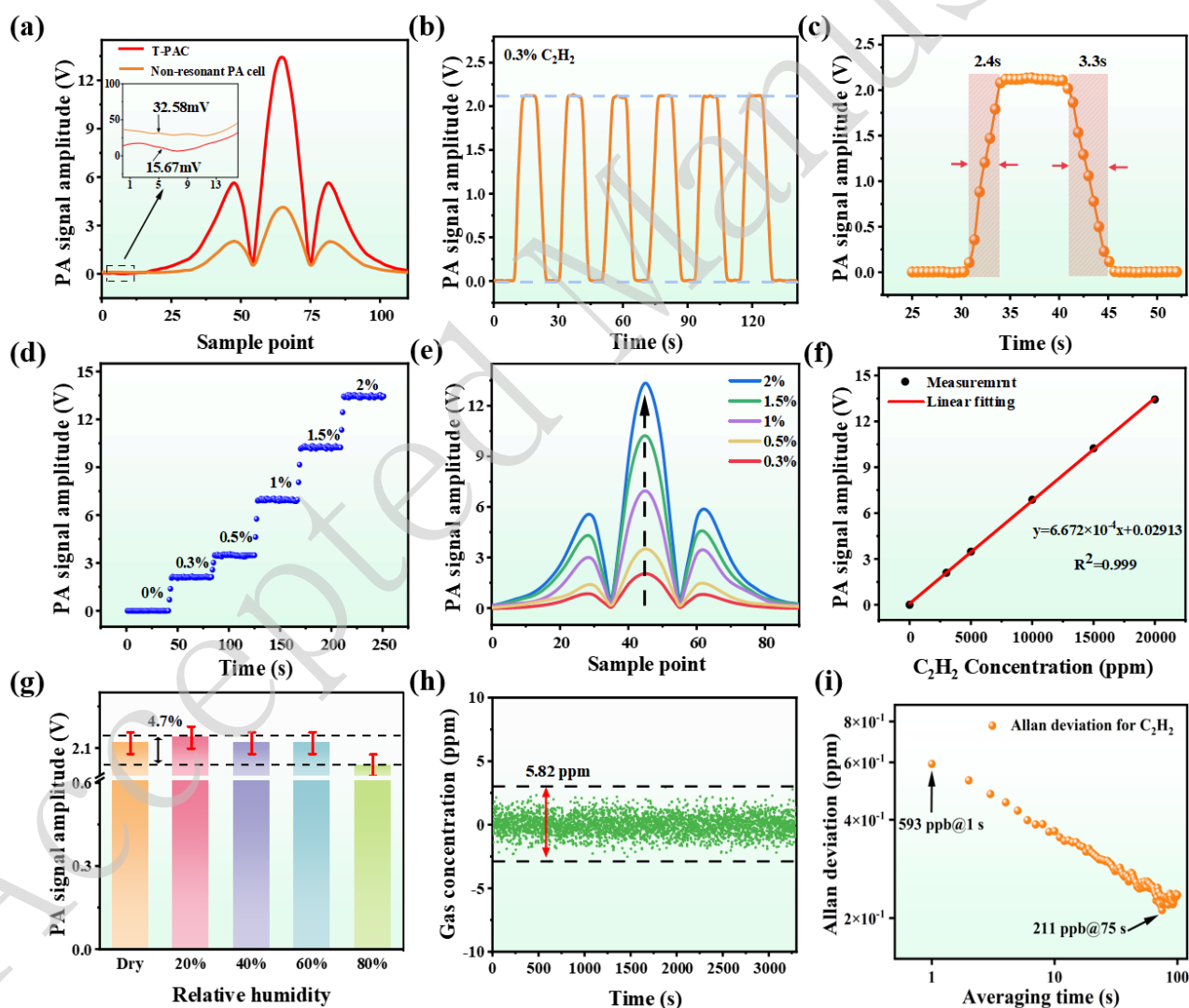


Fig. 5. (a) The $2f$ signal comparison of T-PAC and non-resonant PA cell at a concentration of 2% C_2H_2 gas. (b) Repeatability and response characteristics of the gas sensor at a concentration of 0.3% C_2H_2 gas. (c) Response time testing results of the gas sensor. (d) The PA signal amplitudes at different C_2H_2 gas concentrations. (e) The waveforms of the $2f$ signals at different C_2H_2 gas concentrations. (f) The linear relationship between the PA signal amplitudes and the C_2H_2 gas concentrations. (g) The PA signal amplitudes of 0.3% C_2H_2 gas at different humidity levels. (h) Long-time stability testing of the gas sensor. (i) The variation curve of Allan-Werle deviation versus average time.

Table I Performance comparisons between the proposed photoacoustic sensor and the others.

Ref.	Pump power (mW)	NNEA ($\text{cm}^{-1}\cdot\text{W}\cdot\text{Hz}^{-1/2}$)	OPVR ($\text{mm}\cdot\text{mL}^{-1}$)	Response time (s)	Volume (mL)	Optoelectronic integration
[30]	15.6	5.70×10^{-9}	26.9	-	3	No
[41]	1000	1.84×10^{-8}	3.9	-	204	No
[42]	13	2.27×10^{-9}	0.5	-	102	No
[43]	800	8.18×10^{-8}	3.2	-	52	No
[44]	14.7	1.10×10^{-8}	303.5	-	0.85	No
[45]	20	2.49×10^{-8}	141.7	~63	0.13	No
This work	14	9.46×10^{-9}	1736.8	~3	0.02	Yes

Humidity generator (TAIAN HART, HT0211, China) and calibrated by commercial humidity sensor (TAS-WS-ROC000, China). Fig. 5g shows the measured PA signal amplitudes at different humidity levels, and it can be seen that changes in humidity have little impact on the performance of the gas sensor. The maximum difference is within 4.17%. The stability and detection limit of the developed gas sensor were evaluated at normal temperature and pressure. The long-term stability of the gas sensor was evaluated by introducing pure nitrogen into the T-PAC. As shown in Fig. 5h, the measured gas concentration fluctuates from -2.88 ppm to 2.94 ppm. The detection limit of the gas sensor can be evaluated by Allan-Werle deviation analysis. As shown in Fig. 5i, the detection limit of C_2H_2 gradually decreases with increasing averaging time. When the averaging time is 1 s, the detection limit is 593 ppb. As the averaging time increases, the detection limit can be reduced, and the detection limit is estimated to be 211 ppb for an optimum averaging time of 75 s.

Both the normalized noise equivalent absorption (NNEA) coefficient and the OPVR are key parameters for evaluating the performance of PA gas sensor, which can be expressed by Eq. (6) and Eq. (7)^[39,40], respectively, namely

$$NNEA = \frac{D_L a(v) P}{\sqrt{ENBW}} \quad (6)$$

$$OPVR = \frac{L}{V} \quad (7)$$

where D_L is the detection limit, $a(v)$ is the absorption coefficient, P is the output power of the light source, $ENBW$ is the equivalent noise bandwidth, L and V represent the optical path length and the volume of the PA cell, respectively. In this work, the output power P is about 14 mW, the absorption coefficient $a(v)$ is 0.57 cm^{-1} at 1532.8 nm based on the HITRAN database, the $ENBW$ is 0.25 Hz for 1 s integration time. Therefore, the NNEA coefficient was calculated as $9.46\times 10^{-9} \text{ cm}^{-1}\cdot\text{W}\cdot\text{Hz}^{-1/2}$. In addition, the OPVR can be calculated to be $1736.8 \text{ mm}\cdot\text{mL}^{-1}$. OPVR represents the effective optical pathlength per unit volume of the detection cavity in a PA sensor. Its physical meaning is a core parameter for measuring the interaction

opportunity between light and gas molecules per unit volume. A higher value indicates that under the same cavity volume, the interaction path between light and gas is longer, alternatively, under the same optical pathlength, the required cavity volume is smaller.

To evaluate the performance and innovation of this sensor, table 1 presents the performance of other PA sensors in recent years. The NNEA value of the proposed PA sensor demonstrates moderate performance compared to others, primarily due to the trade-off between integration level and sensitivity. The further improvement of the NNEA value can be achieved by increasing the optical path length. It is worth mentioning that the proposed T-PAC has a very small volume of only 0.02 mL, the OPVR of the sensor is $1736.8 \text{ mm}\cdot\text{mL}^{-1}$, which is higher than that of other types of sensors, indicating that the proposed sensor can achieve a longer optical path in a unit volume and maintain high performance in a compact volume. In addition, the proposed sensor has shorter response time and higher integration compared to other sensors, making it more suitable for practical applications.

Discussion

In conclusion, this paper developed a miniaturized PA gas sensor based on the multimaterial optoelectronic fiber. The optoelectronic fibers were fabricated by a scalable thermal drawing technique. The T-PAC was designed and integrated on the tip of the fiber to realize simultaneous transmission of light signals and electrical signals, which avoids the disadvantages of traditional PA gas sensors such as bulky size and non-integration. Meanwhile, the size of the T-PAC was optimized by balancing the volume and sensitivity of the sensor. C_2H_2 gas was selected as the target gas to evaluate the performance of the proposed sensor. Compared to the PA gas sensor with non-resonant PA cell at the same size, the SNR of the proposed PA gas sensor with T-PAC was improved by a factor of 7.0. The sensor shows a high sensitivity with a response rate of 0.667 mV/ppm when the lock-in integration time is 1 s. The Allan-Werle deviation analysis results show that the sensor has a detection limit of 593 ppb for

an average of 1 s, and the detection limit is reduced to 211 ppb at an averaging time of 75 s. The total volume of the sensor is only 0.02 mL, which is much smaller than that of the traditional PA gas sensors. Therefore, the sensor can adapt to narrower environments. At the same time, by changing the laser, it can be extended to a variety of gas detection. The experimental results demonstrate the excellent performance of the developed gas sensor, which has great potential for applications in industrial safety, environmental monitoring and healthcare.

Materials and methods

Fabrication of optoelectronic fibers

The multimaterial optoelectronic fibers were fabricated using a glass fiber and two copper electrodes as the core components, with PMMA as the cladding. A PMMA rod (30 mm diameter, 12 cm length) was prepared with one central hole (8 mm diameter, 12 cm length) and two side holes (3 mm diameter), positioned symmetrically 5 mm from the central axis.

The preform was thermally drawn using a three-zone furnace at $160\pm 5^\circ\text{C}$ (top), $250\pm 10^\circ\text{C}$ (middle), and $120\pm 5^\circ\text{C}$ (bottom). The feeding and drawing speed were 1 ± 0.1 mm/min and 2 ± 0.1 m/min, respectively. During the drawing process, two copper electrodes wires (with diameters of 50 μm) and one glass fiber (with a diameter of 125 μm) were continuously inserted into the respective holes. The fiber diameter was monitored in real time by a laser rangefinder.

Gas sensing system

A distributed feedback (DFB) diode laser was used as the light source, and its temperature and current were controlled using a laser driver (Thorlabs, CLD1015, USA). A signal generator (Gwinstek, MFG-2260M, Taiwan) produced a combined signal consisting of a periodic triangular scanning wave signal and a periodic sinusoidal wave modulation signal to drive the laser by the laser driver. The frequency of the sinusoidal wave signal was set to half the resonant frequency of the T-PAC. The modulated pump light from the DFB laser was directed through a multimaterial optoelectronic fiber into the T-PAC, where it interacted with the target gas to generate a periodic PA signal. The PA signal was detected by a miniature MEMS microphone, then converted into an electrical signal, and finally transmitted via a copper wire to a lock-in amplifier (Stanford Research Systems, SR860, USA), the lock-in amplifier has an integrated preamplifier and bandpass filter inside, which can effectively extract weak signals while suppressing noise and interference. The lock-in amplifier extracted the $2f$ signals, which is proportional to the gas concentrations. To prepare the desired target concentrations of C_2H_2 gas, standard concentrations of C_2H_2 and nitrogen gas were mixed using a mass flow control (MFC).

Acknowledgements

This work was supported by the National Natural Science Foundation of China (No. 62035006, 62405111), the Program of Marine Economy Development Special Fund (six marine industries) under Department of Natural Resources of

Guangdong Province (No. GDNRC [2024]16), the Guangdong Basic and Applied Basic Research Foundation (No. 2025A1515010112, 2023A1515110071), the National Key Research and Development Program of China (No. 2024YFE0209200), the Guangzhou Science and Technology Project (No. 2025A04J2279), the Fundamental Research Funds for the Central Universities (No. 21624346).

Conflict of Interest

The authors declare no conflict of interest.

Author Contributions

Yanyu Jiang, Minghui Du and Xile Han contributed equally to this work. Yanyu Jiang: Investigation, Writing - original draft Preparation. Minghui Du: Writing - original draft Preparation, Supervision. Xile Han: Writing - original draft Preparation. Zhuobei Deng: Investigation, Conceptualization. Jie Mao: Investigation. Liang Chen: Investigation. Yifan Wang: Investigation. Ying Liu: Investigation. Yafei Li: Conceptualization, Investigation, Writing - Review & Editing. Ruohui Wang: Writing - Review & Editing. Chuantao Zheng: Writing - Review & Editing. Tuan Guo: Writing - Review & Editing, Funding acquisition.

Data Availability Statement

The data that support the findings of this study are available from the corresponding author upon reasonable request.

References

- [1] Mei, W. X. et al. Operando monitoring of thermal runaway in commercial lithium-ion cells via advanced lab-on-fiber technologies. *Nature Communications* **14**, 5251 (2023).
- [2] Xue, X. B. et al. Operando battery monitoring: lab-on-fiber electrochemical sensing technologies. *Laser & Photonics Reviews* **18**, 2301298 (2024).
- [3] Liu, P. et al. Revealing lithium battery gas generation for safer practical applications. *Advanced Functional Materials* **32**, 2208586 (2022).
- [4] Qi, H. C. et al. Rapid photoacoustic exhaust gas analyzer for simultaneous measurement of nitrogen dioxide and sulfur dioxide. *Analytical Chemistry* **96**, 5258-5264 (2024).
- [5] Ma, Y. F. et al. Design of multipass cell with dense spot patterns and its performance in a light-induced thermoelastic spectroscopy-based methane sensor. *Light Advanced Manufacturing* **6**, 5-13 (2025).
- [6] Shende, P. et al. Systematic approaches for biodiagnostics using exhaled air. *Journal of Controlled Release* **268**, 282-295 (2017).
- [7] Heng, W. Z. et al. Exhaled breath analysis: from laboratory test to wearable sensing. *IEEE Reviews in Biomedical Engineering* **18**, 50-73 (2025).
- [8] Gong, C. Y. et al. Submonolayer biolasers for ultrasensitive biomarker detection. *Light: Science & Applications* **12**, 292 (2023).
- [9] Sun, H. Y. et al. Parts-per-quadrillion level gas molecule detection: CO-LITES sensing. *Light: Science & Applications* **14**, 180 (2025).

- [10] Wu, G. J. et al. PET-cantilever-enhanced fiber-optic photoacoustic spectroscopy for rapid Subppm methane detection. *Analytical Chemistry* **97**, 15510-15515 (2025).
- [11] Wu, G. J. et al. A dual-enhancement fiber-optic photoacoustic spectroscopy sensor based on a spherical-cylindrical coupled resonator with an integrated multipass cell for sub-ppb C₂H₂ detection. *Analytical Chemistry* **97**, 20543-20548 (2025).
- [12] Shi, J. et al. Hybrid optical parametrically-oscillating emitter at 1930 nm for volumetric photoacoustic imaging of water content. *eLight* **2**, 6 (2022).
- [13] Fathy, A. et al. Direct absorption and photoacoustic spectroscopy for gas sensing and analysis: a critical review. *Laser & Photonics Reviews* **16**, 2100556 (2022).
- [14] Gong, Z. F. et al. Integration of T-type half-open photoacoustic cell and fiber-optic acoustic sensor for trace gas detection. *Optics Express* **27**, 18222-18231 (2019).
- [15] Li, C. L. et al. High-speed multi-pass tunable diode laser absorption spectrometer based on frequency-modulation spectroscopy. *Optics Express* **26**, 29330-29339 (2018).
- [16] Zhao, X. Y. et al. Ultra-high sensitive photoacoustic gas detector based on differential multi-pass cell. *Sensors and Actuators B: Chemical* **368**, 132124 (2022).
- [17] Ma, J. et al. Microscale fiber photoacoustic spectroscopy for *in situ* and real-time trace gas sensing. *Advanced Photonics* **6**, 066008 (2024).
- [18] Karhu, J. et al. Sub-ppb detection of benzene using cantilever-enhanced photoacoustic spectroscopy with a long-wavelength infrared quantum cascade laser. *Optics Letters* **45**, 5962-5965 (2020).
- [19] Ktafi, I. et al. A new approach toward extreme thermal stability of femtosecond laser induced modifications in glasses. *Laser & Photonics Reviews* **19**, 2401086 (2025).
- [20] Du, M. H. et al. Multimaterial fibers for multifunctional sensing applications. *Laser & Photonics Reviews* **18**, 2301125 (2024).
- [21] Yan, W. et al. Advanced multimaterial electronic and optoelectronic fibers and textiles. *Advanced Materials* **31**, 1802348 (2019).
- [22] Jiang, H. et al. Optical fibre based artificial compound eyes for direct static imaging and ultrafast motion detection. *Light: Science & Applications* **13**, 256 (2024).
- [23] Leber, A. et al. Highly integrated multi-material fibers for soft robotics. *Advanced Science* **10**, 2204016 (2023).
- [24] Zhou, X. H. et al. Fiber crossbars: an emerging architecture of smart electronic textiles. *Advanced Materials* **35**, 2300576 (2023).
- [25] Dang, C. et al. Fibres-threads of intelligence-enable a new generation of wearable systems. *Chemical Society Reviews* **53**, 8790-8846 (2024).
- [26] Wang, Z. X. et al. High-quality semiconductor fibres via mechanical design. *Nature* **626**, 72-78 (2024).
- [27] Richard, I. et al. Unraveling the influence of thermal drawing parameters on the microstructure and thermo-mechanical properties of multimaterial fibers. *Small* **18**, 2101392 (2022).
- [28] Tam, A. C. Applications of photoacoustic sensing techniques. *Reviews of Modern Physics* **58**, 381-431 (1986).
- [29] Li, Y. F. et al. Double resonant cavity enhanced photoacoustic gas sensor for acetylene detection. *IEEE Transactions on Instrumentation and Measurement* **74**, 7000208 (2025).
- [30] Zhang, M. et al. A high-sensitivity compact dual-T-type resonant fiber-optic photoacoustic sensor for simultaneous detection of multiple gases. *Sensors and Actuators B: Chemical* **418**, 136328 (2024).
- [31] Zhang, B. et al. Flexible hollow core fiber photoacoustic gas sensor based on embedded acoustic resonant structure. *Analytical Chemistry* **95**, 12761-12767 (2023).
- [32] Bijnen, F. G. C., Reuss, J. & Harren, F. J. M. Geometrical optimization of a longitudinal resonant photoacoustic cell for sensitive and fast trace gas detection. *Review of Scientific Instruments* **67**, 2914-2923 (1996).
- [33] Faccini de Lima, C. et al. Multimaterial fiber as a physical simulator of a capillary instability. *Nature Communications* **14**, 5816 (2023).
- [34] Chen, X. et al. Thermally drawn multi-material fibers: from fundamental research to industrial applications. *National Science Review* **11**, nwae290 (2024).
- [35] Wang, Z. et al. Designer patterned functional fibers via direct imprinting in thermal drawing. *Nature Communications* **11**, 3842 (2020).
- [36] Gupta, N. et al. A single-fibre computer enables textile networks and distributed inference. *Nature* **639**, 79-86 (2025).
- [37] Zhang, B. et al. Low-frequency resonant photoacoustic gas sensor by employing hollow core fiber-based O-shaped multipass cells. *Analytical Chemistry* **95**, 12811-12818 (2023).
- [38] Xu, S. Y. et al. Photoacoustic spectroscopy based on vertical cruciform multi-stepped photoacoustic cell achieving ppb-level acetylene detection. *Sensors and Actuators B: Chemical* **418**, 136313 (2024).
- [39] Zhao, P. C. et al. Ultraminiature optical fiber-tip 3D-microprinted photothermal interferometric gas sensors. *Laser & Photonics Reviews* **18**, 2301285 (2024).
- [40] Qiao, S. D. et al. Ultra-highly sensitive dual gases detection based on photoacoustic spectroscopy by exploiting a long-wave, high-power, wide-tunable, single-longitudinal-mode solid-state laser. *Light: Science & Applications* **13**, 100 (2024).
- [41] Ma, Y. F. et al. Highly sensitive acetylene detection based on multi-pass retro-reflection-cavity-enhanced photoacoustic spectroscopy and a fiber amplified diode laser. *Optics Express* **27**, 14163-14172 (2019).
- [42] Zhang, G. Y. et al. Miniature 3D-printed resonant photoacoustic cell for flowing gas detection. *Sensors and Actuators A: Physical* **341**, 113594 (2022).
- [43] Wang, Q. Y. et al. High-precision detection of acetylene using photoacoustic spectroscopy with a three-step cylindrical cell. *IEEE Sensors Journal* **24**, 20719-20725 (2024).
- [44] Chen, K. et al. Highly sensitive photoacoustic gas sensor based on multiple reflections on the cell wall. *Sensors and*

Actuators A: Physical **290**, 119-124 (2019).

- [45] Guo, M. et al. Miniaturized anti-interference cantilever-enhanced fiber-optic photoacoustic methane sensor. *Sensors and Actuators B: Chemical* **370**, 132446 (2022).

Accepted Manuscript